Epoxy Toughening with Low Graphene Loading

Yong Tae Park, Yuqiang Qian, Clement Chan, Taewon Suh, Mehrdad Ghasemi Nejhad, Christopher W. Macosko, and Andreas Stein**

The toughening effects of graphene and graphene-derived materials on thermosetting epoxies are investigated. Graphene materials with various structures and surface functional groups are incorporated into an epoxy resin by in situ polymerization. Graphene oxide (GO) and GO modified with amine-terminated poly(butadiene-acrylonitrile) (ATBN) are chosen to improve the dispersion of graphene nanosheets in epoxy and increase their interfacial adhesion. An impressive toughening effect is observed with less than 0.1 wt% graphene. A maximum in toughness at loadings as small as 0.02 wt% or 0.04 wt% is observed for all four types of graphene studied. An epoxy nanocomposite with ATBN-modified GO shows a 1.5-fold improvement in fracture toughness and a corresponding 2.4-fold improvement in fracture energy at 0.04 wt% of graphene loading. At such low loadings, these graphene-type materials become economically feasible components of nanocomposites. A microcrack mechanism is proposed based on microscopy of the fracture surfaces. Due to the stress concentration by graphene nanosheets, microcracks may be formed to absorb the fracture energy. However, above a certain graphene concentration, the coalescence of microcracks appears to facilitate crack propagation, lowering the fracture toughness. Crack deflection and pinning likely contribute to the slow increase in fracture toughness at higher loadings.

1. Introduction

Epoxy polymers are widely used as adhesives, coatings, and structural materials. As thermosetting materials, epoxies exhibit a high degree of crosslinking, which endows them with useful properties, such as high rigidity and strength. However, the crosslinked structure also makes epoxies intrinsically brittle and vulnerable to cracks, which limits their applications in aerospace or automotive parts. It is therefore of great interest to improve the fracture toughness of epoxies. Traditionally applied tougheners, such as liquid rubbers[1,2] and thermoplastic polymers,[3] can increase the toughness of epoxies by forming micrometer-sized secondary phases, but typically, 5–20 wt% of toughener is required, causing a noticeable reduction in modulus and a suppression of glass transition temperatures. Inorganic nanofillers, such as metal oxides, nanoclays, and carbon nanomaterials, have also been extensively studied to improve the fracture toughness of epoxies.[4–6] Different from polymeric tougheners, increases in the modulus and glass transition temperatures are often observed due to the high stiffness of inorganic nanofillers. However, the increase in fracture toughness obtained with inorganic nanofillers is typically less than that with polymeric tougheners.

Graphene consists of a single layer of carbon atoms and has recently emerged as a promising material for polymer nanocomposites, energy storage and electronics applications, due to its unique structure and its excellent mechanical and electrical properties.[7,8] The introduction of graphene nanosheets into polymers resulted in improved mechanical, electrical, and barrier performances. Because of the high aspect ratio of graphene nanosheets, the property enhancements can be obtained at relatively small loadings, in some cases less than 0.5 wt%.[7,9,10] For epoxy toughening, Rafiee et al. compared the fracture performance of epoxy composites with 0.1 wt% of pristine graphene, single-walled and multi-walled carbon nanotubes, and demonstrated that the composites with graphene showed the highest fracture toughness.[11] They also found that the improvement in fracture toughness peaked at 0.125 wt% of graphene with a 65% increase.[12] Since many industrial applications of graphene are still limited by its relatively high cost, the improvements at low loadings of graphene provide opportunities to produce cost-effective epoxy/graphene nanocomposites. Epoxy nanocomposites with surface functionalized graphene and graphene oxide (GO) were also studied, and the fracture toughness increased with graphene loading.[6,13] However, most of these studies used solvents and dispersions with relatively high graphene loadings, which places limitations on industrial implementation.

Dr. Y. T. Park,[+] T. Suh, Prof. C. W. Macosko
Department of Chemical Engineering
& Materials Science
University of Minnesota
421 Washington Ave. SE, Minneapolis, MN 55455, USA
E-mail: macosko@umn.edu
Dr. Y. Qian,[++] C. Chan, Prof. A. Stein
Department of Chemistry
University of Minnesota
207 Pleasant St. SE, Minneapolis, MN 55455, USA
E-mail: a-stein@umn.edu
Prof. M. G. Nejhad
Department of Mechanical Engineering
University of Hawaii at Manoa
2540 Dole St., Honolulu, HI 96822, USA

[+] Present address: Department of Mechanical Engineering, Myongji University, 116 Myongji-ro, Cheoin-gu, Yongin, Gyeonggi-do, 449–728, Korea
[++] Present address: The H.B. Fuller Company, 1200 Willow Lake Blvd, St. Paul, MN 55110, USA

DOI: 10.1002/adfm.201402553

Motivated by the above results, we sought to investigate the toughening effects of graphene nanosheets in bulk-polymerized epoxy nanocomposites. The content of graphene in the nanocomposites was kept lower than 0.3 wt%.[14] In addition, no solvent was used in the nanocomposite preparation. Pristine graphenes, GO, and surface-modified GO were employed to prepare epoxy nanocomposites. The toughening effects of different graphene materials were demonstrated at loadings less than 0.1 wt%. Interestingly, a maximum toughening effect was observed at 0.02 wt% or 0.04 wt% of graphene loading for all the composite samples, and GO modified with specific surface groups outperformed the pristine graphenes and GO. Fractographs of the composite samples were collected to investigate the toughening mechanism. A mechanism is proposed to explain the fracture behavior of polymer composites with low loading levels of graphene.

2. Results and Discussion

2.1. Modification of Graphene Oxide

In this study, we prepared a new class of highly toughened epoxy composites from amine-terminated poly(butadiene-acrylonitrile) (ATBN)-modified GO (GA) where the covalently bonded strong interface plays an important role in fracture characteristics. ATBN chains were grafted onto GO using 4,4′-methylene diphenyl diisocyanate (MDI) as the coupling agent, as illustrated in **Figure 1**.

Figure 2 shows the Fourier transform-infrared (FT-IR) spectra for GO and modified GOs. During the Hummers oxidation of graphite, the conjugated carbon lattice is attacked by strong oxidants, such as potassium permanganate and nitric acid. Structural defects are created subsequently and oxygen-containing groups decorate the surfaces or edges of the nanosheets.[15] The resulting GO has a C/O atomic ratio of 2:1 as confirmed by XPS (Figure S13 in Supporting Information), and the oxygens are present principally as epoxide groups with fewer hydroxide groups.[16] Strong O–H absorption bands were observed for GO from 3000 to 3700 cm^{-1}. Peaks corresponding to O–H bending, C=O and C=C stretching vibrations are also clearly seen in Figure 2.[17] Organic isocyanates were reported to react with the hydroxyl groups on GO,[18] so here di-isocyanate MDI was used to create –NCO groups on GO. The resulting isocyanate-modified GO (GO-NCO) showed an absorption peak corresponding to –NCO groups at 2269 cm^{-1}, indicating the successful grafting of –NCO groups on GO. The weak intensity of the –NCO peak is due to the consumption of –NCO groups by moisture during the preparation of the FT-IR specimen of GO-NCO. In order to avoid the reaction with moisture, GO-NCO was not dried in air, but immediately after washing with dichloromethane it was directly dispersed in dimethylformamide (DMF) for the following reaction with ATBN. The spectrum in Figure 2 of the resulting GA shows C–H vibrations at 2850 cm^{-1} and 2920 cm^{-1} from the grafted ATBN chains. The –NCO signal from GO-NCO disappeared in GA, confirming the reaction between –NCO groups on GO-NCO and the amine groups on ATBN. Some of the original O–H and C=O groups are maintained even after the modification process, according to the FT-IR spectra.

Graphite consists of closely stacked graphene sheets with an interlayer spacing of 0.355 nm. The Hummers oxidation process created hydroxyl and epoxide groups on GO nanosheets,[15] so the *d*-spacing of GO increased to 0.74 nm, as shown in **Figure 3**. After surface modification, the *d*-spacing increased to 1.10 nm for GO-NCO and 1.38 nm for GA, consistent with the attachment of functional groups to the GO surfaces. The increase in *d*-spacing from GO to GO-NCO is greater than that from GO-NCO to GA, probably because the molecular structure of the aromatic MDI group is more rigid than the aliphatic ATBN chain.

Thermogravimetric analysis (TGA) was used to determine the content of organic functional groups on GA. As shown in **Figure 4**, GO displays a major weight loss of 30% from 150 °C to 250 °C, which is due to the decomposition of labile surface hydroxyl groups. As for GA, two weight loss processes were

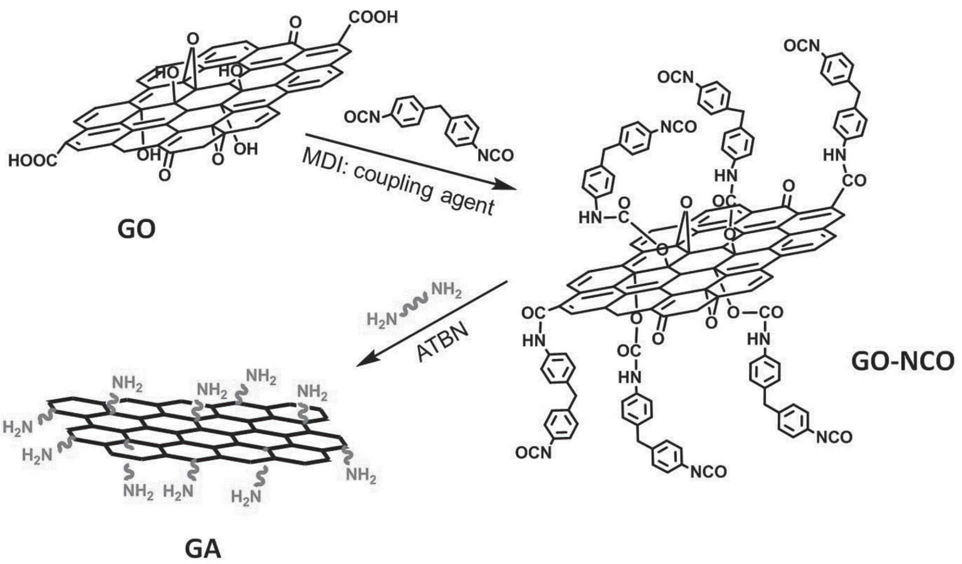

Figure 1. Scheme illustrating the modification of GO with ATBN molecules. The di-isocyanate linkage in GA is omitted for clarity.

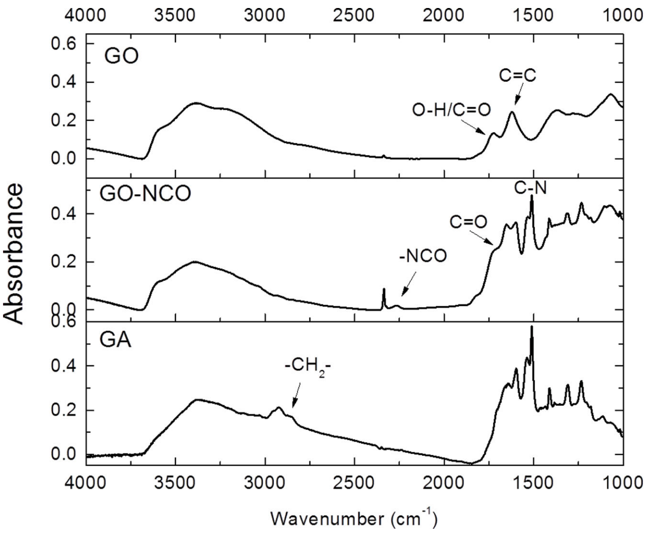

Figure 2. FT-IR spectra of GO, GO-NCO, and GA.

observed from the derivative TGA curve. The first weight loss with a derivative TGA peak at 175 °C was assigned to the loss of surface hydroxyl groups, similar to the one in GO. The second weight loss with a broad peak in the derivative TGA curve at 370 °C was assigned to the loss of covalently bonded organic functional groups. The organic content of GA was calculated to be 26.5 wt% from the second weight loss of GA. By considering this value together with the densities of GO and ATBN, one can estimate the average thickness of the ATBN layer to be 0.34 nm on each sheet surface, consistent with the observed change in *d*-spacing from GO to GA.

2.2. Morphology of Graphene Nanofillers

Besides GO and GA, two grades of pristine graphene nanosheets, GS1 and GS2, were also used in this study, and their specifications are listed in **Table 1** according to the manufacturer. The morphologies of the graphene nanofillers were characterized by electron microscopy. In transmission electron microscopy (TEM) images in **Figure 5**, all the graphene materials are observed as thin nanosheets with sizes of several micrometers. The wrinkled morphology of GS2, GO, and GA is due to the flexibility of the 2D nanosheets. However, fewer wrinkles are observed for GS1 in Figure 5a, because the stacking of many graphene layers in GS1 makes it graphite-like and thus more rigid than individual nanosheets.

Bulk morphologies of the obtained graphene powders were revealed by scanning electron microscopy (SEM). The pristine graphene samples, GS1 and GS2, were received as fluffy powders. In **Figure 6**, GS1 exhibits a flake-like morphology similar to that seen in the TEM image (Figure 5a), whereas the thin graphene sheets of GS2 have a wrinkled/corrugated morphology due to their high flexibility. As for GO, it is difficult to obtain these powders in bulk form by filtering the GO dispersion, because GO nanosheets block the pores of the membrane filter. Also, by filtration, GO was obtained as a stacked and dense paper,[19] which would be hard to disperse in the amine curing agent. Freeze-drying, a simple and scalable method to separate nanoparticles from their dispersions,[20] was used instead to keep graphene sheets from aggregating. The SEM images of GO and GA after freeze-drying are shown in Figure 6c,d, respectively. It can be clearly seen that the nanosheets still maintain high aspect ratios, and there is no substantial stacking of the sheets.

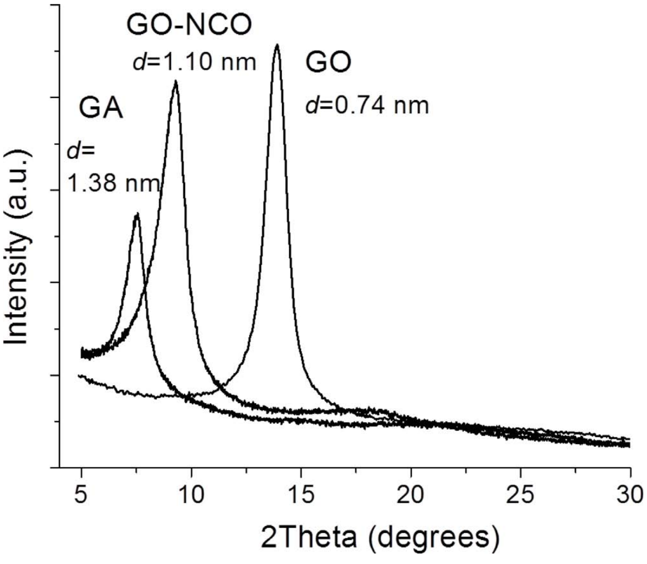

Figure 3. X-ray diffraction (XRD) patterns of GO, GO-NCO, and GA. X-ray source: Co anode.

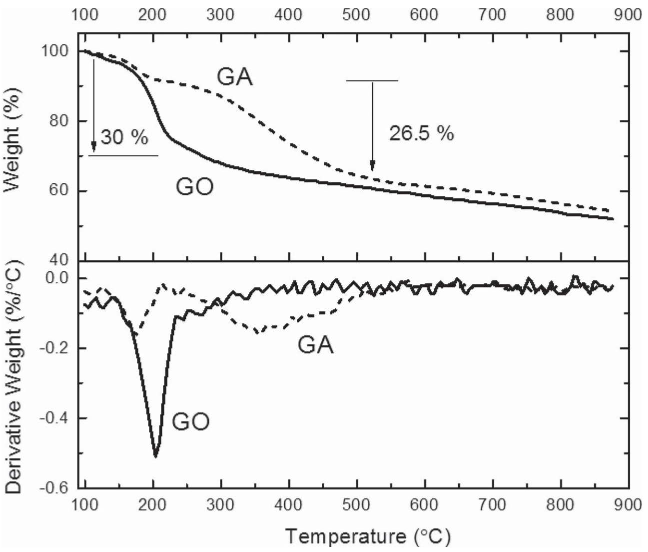

Figure 4. TGA and first derivative TGA curves of GO and GA from room temperature to 900 °C in nitrogen.

Table 1. Specifications of pristine graphene nanosheets from the manufacturer.

Notation	Product name	Thickness	Size	Oxygen content	Surface area
GS1	N006-P	10–20 nm	≈14 μm	1.5%	≤21 m^2 g^{-1}
GS2	N002-PDR	<1 nm	≤10 μm	2.1%	400–800 m^2 g^{-1}

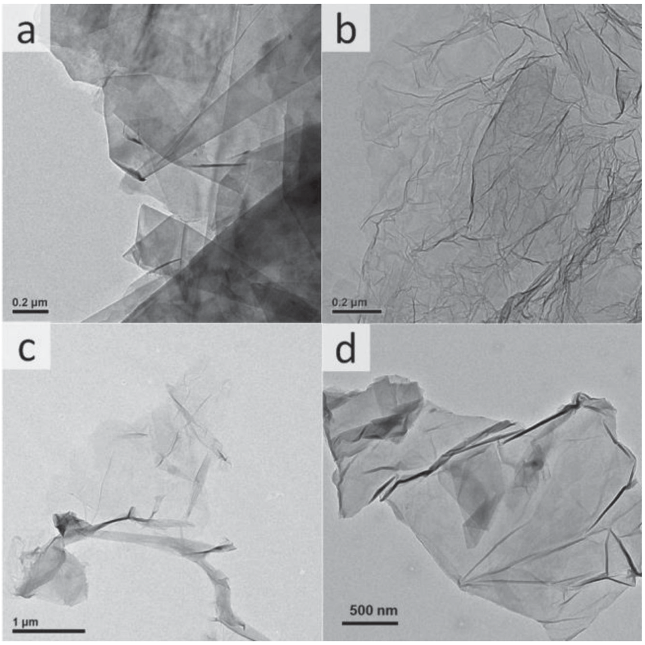

Figure 5. TEM images of a) GS1, b) GS2, c) GO, and d) GA. Specimens were prepared from ethanol a,b,c) or DMF d) dispersion.

2.3. Dispersion of Graphene Nanofillers

Because Jeffamine D230 curing agent is much less viscous than the epoxy resin, graphene nanofillers were first dispersed in the curing agent by ultrasonication. The resulting blends were denoted as D_graphene_*x*, where *x* is the graphene weight percentage in the dispersion. All D_graphene dispersions were pourable at room temperature, and they had fluid-like behavior with very low viscosity as shown in **Figure 7**. Figure 7a,b show the viscosity of D230 and graphene dispersions via mixing and ultrasonication as a function of shear rate and shear stress, respectively. With GS1 and GS2, the dispersions showed shear thinning, whereas Newtonian behavior was observed for neat D230 and the dispersions with GO and GA. Shear thinning was the result of swelling of graphene by the D230 and formation of a 3-dimensional network of graphene nanosheets within the D230 matrix, similar to the behavior of clay nanosheets in polyols we have observed previously.[21] The viscosity dramatically increased by addition of the thinner, fewer-layered graphene nanosheets, GS2, dispersions of which showed stronger shear thinning than those with GS1. On the other hand, D230 with GO or GA showed only a small increase in viscosity, indicating that these nanofillers were not exfoliated but remained in the form of thick layered stacks.

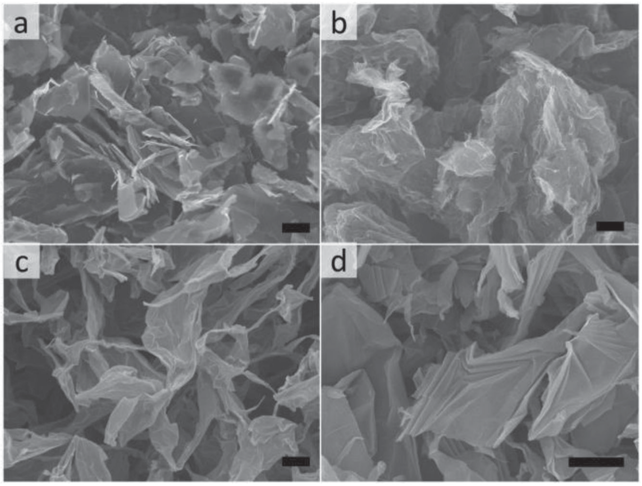

Figure 6. SEM images of a) GS1, b) GS2, c) GO, and d) GA powders. GS1 and GS2 specimens were prepared as received from the manufacturer, and GO and GA specimens were prepared after freeze-drying. Scale bar: 2 μm.

The dispersion state of graphene nanofillers in the final epoxy polymer is greatly affected by the compatibility between epoxy/amine and the surface of different graphene materials. The final nanocomposites were denoted as E_graphene_*y*, where *y* is the graphene weight percentage in the nanocomposite. For example, the D_graphene_1.16 dispersion was mixed with epoxy resin at a D230:epoxy resin weight ratio of 35:100 to make the final composite, E_graphene_0.30. The TEM images in **Figure 8** illustrate the state of dispersion of nanofiller particles in the epoxy matrix. Good dispersions of high-aspect-ratio graphene nanosheets can be observed for E_GS1 (Figure 8a) and E_GS2 (Figure 8b). The thickness values of typical nanosheets were ≈15 nm and 3 nm for GS1 and GS2, respectively, on the basis of TEM images. Similar to the TEM images of pristine graphenes (Figure 6), GS1 displays less corrugation than GS2 due to the high rigidity of the multilayered nanosheets. Despite the good dispersity of GO in water, the dense stacking of GO nanosheets is clearly seen in E_GO even after intense ultrasonication treatment (Figure 8c). The aggregation of GO nanosheets resulted from the unmatched surface properties between hydrophilic GO and the D230/epoxy matrix. After modification with ATBN, intercalation and exfoliation of GA was observed in E_GA (Figure 8d). Typical thicknesses of GO and GA sheets in the nanocomposites are ≈30 nm and 10 nm, respectively, estimated from TEM.

2.4. Thermo-mechanical Properties and Fracture Toughness of Epoxy Nanocomposites

Thermo-mechanical properties of E_graphene composites were studied by dynamic mechanical analysis (DMA). The addition of 0.08 and 0.16 wt% of graphene to epoxy induced only a small increase in tensile storage modulus, E', as shown in **Figure 9**a (and Figure S1 in Supporting Information). As shown in Figure 9b, E_GS1 and E_GS2 exhibited maximum E'' values at the same temperature as neat epoxy, whereas E_GO showed the maximum E'' at higher temperature due to the strong epoxy-GO interfaces. The E_GA nanocomposite displayed the maximum E'' value at the lowest temperature among all nanocomposites, which could be the result of the addition of grafted rubber chains on graphene surfaces.

The results from differential scanning calorimetry (DSC) measurements showed a similar trend to those from DMA. At a 0.16 wt% graphene loading, E_GO exhibited the highest glass transition temperature, T_g, and E_GA the lowest T_g. Storage

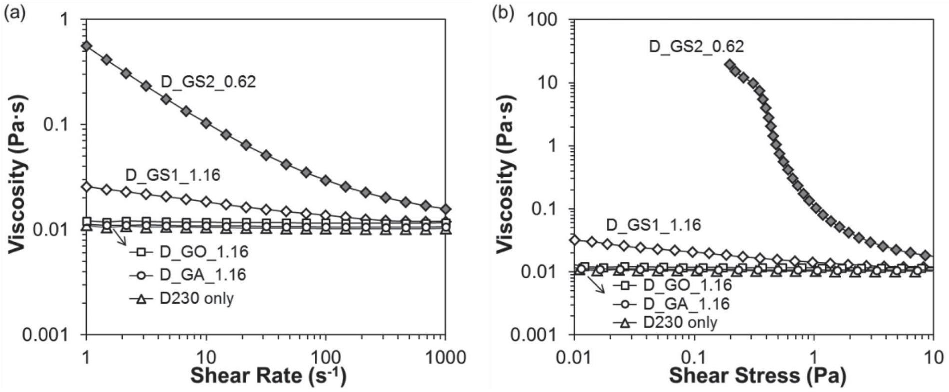

Figure 7. Steady shear viscosity of D230 dispersions with 1.16 wt% graphene. The dispersion with 1.16 wt% GS2 is a viscous paste.

tensile moduli, E', and T_g of neat epoxy and epoxy nanocomposites are listed in **Table 2.** T_g was estimated from the temperature at maximum tan δ ($=E'/E''$) as well as maximum loss modulus E''. T_g values from DSC analysis are also listed. A reduction of T_g, which is typically found in epoxy toughening by liquid rubbers or thermoplastic polymers,[1] is absent. Rather, a small increase was observed, similar to other studies with graphene and epoxy.[10]

Flexural modulus and strength of the epoxy/graphene nanocomposites are shown in **Figure 10** (typical data are shown in Figure S2 in Supporting Information). The moduli of epoxy nanocomposites with pristine graphenes fluctuate as a function of graphene contents from 0.01 to 0.3 wt%. The insignificant effect of pristine graphenes on modulus change is due to the weak epoxy-graphene interface, resulting from the inert graphene lattice on the surface of GS1 and GS2. E_GO also displayed negligible change in modulus compared to the neat epoxy, because of the aggregation of GO nanosheets in the epoxy matrix. A slight increase in modulus was observed for E_GA and was attributed to the good dispersion of GA nanosheets as well as the covalently bonded GA/epoxy interface. Tensile modulus data vs graphene loading fit the Mori–Tanaka model (see Figure S1 in Supporting Information).[22] All the epoxy nanocomposites showed a slight decrease in tensile strength (Figure S3 in Supporting Information), which is commonly observed for polymer nanocomposites with stiff nanofillers. However, overall the mechanical modulus and strength of the epoxy matrix are not highly responsive to the incorporation of graphene nanofillers.

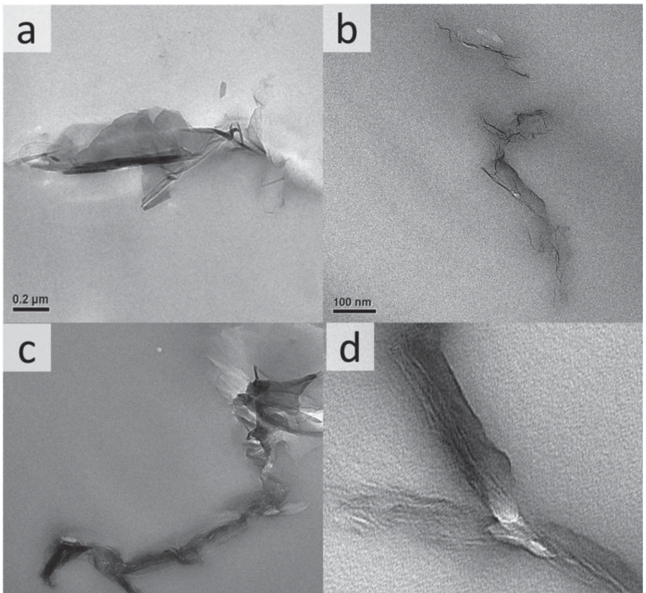

Figure 8. TEM images of epoxy nanocomposites with 0.16 wt% of a) GS1, b) GS2, c) GO, and d) GA.

Graphene nanofillers have a more significant impact on the fracture toughness and fracture energy of the epoxy matrix, as shown in Figure 10c,d. Crack-opening tests on compact tension samples were performed to measure the mode-I critical stress intensity factor (K_{Ic}, fracture toughness) and critical strain energy release rate (G_{Ic}, fracture energy) of the pure epoxy matrix and E_GS, E_GO and E_GA nanocomposites at various weight fractions of graphenes (see Figure S2b in Supporting Information). The K_{Ic} of the neat epoxy, 0.97 MPa m$^{1/2}$, is in good agreement with other neat epoxy polymers in previous studies.[11,12] For E_GS1, the K_{Ic} increased by 35% with only 0.02 wt% of graphene loading, compared to the base value of the epoxy. A sharp decrease of K_{Ic} was observed at 0.04 wt% of graphene loading, which was followed by a trend of slow increase upon higher graphene loadings (also in **Figure 11**). Surprisingly, similar peak behavior in the toughening effect can also be seen in Figure 10c for the composites with other graphene nanofillers at 0.02 wt% or 0.04 wt% graphene loading, and the maximum improvements of K_{Ic} were 32%, 40% and 52% for E_GS2, E_GO and E_GA, respectively. The best performance of E_GA is attributed to the good dispersion of GA and the strong epoxy-GA interface in the nanocomposites. Correspondingly, E_GA displayed a maximum 2.4-fold improvement in G_{Ic} at 0.04 wt% of graphene loading. In this study, all K_{Ic} and G_{Ic} data exhibited experimental errors of 8.3% and 24.1%, respectively, on average. It is normal to have a relatively large measurement error in fracture tests. The error we observed in the fracture toughness measurements is comparable to or smaller than that in many other publications (see Table S2 in Supporting Information).

A maximum in epoxy toughening at small graphene loadings was reported in a previous study on graphene-based epoxy

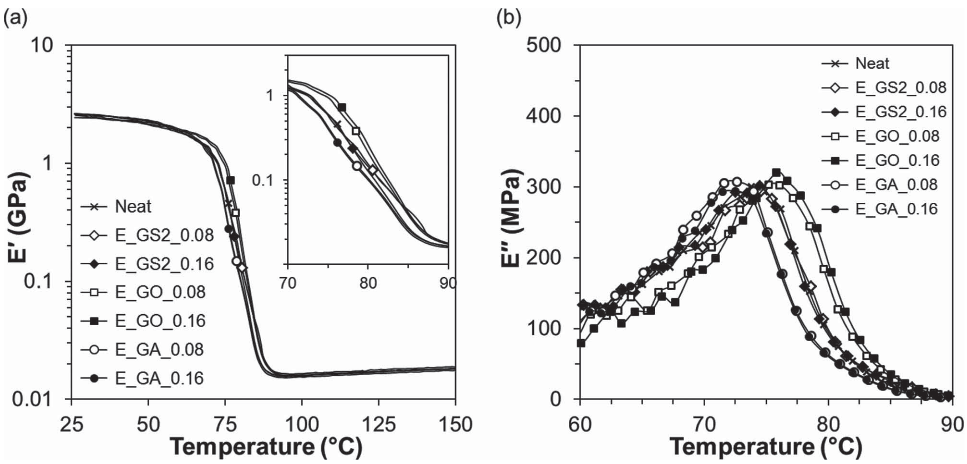

Figure 9. Dynamic mechanical analysis of the neat epoxy and epoxy/graphene nanocomposites: a) storage modulus, *E′*, and b) loss modulus, *E″*.

composites, but at a larger graphene loading (>0.1 wt%) than those shown here.[12] In contrast, continuous toughening with the increase of graphene loading was reported in several other studies, but they required at least 10-times higher loadings of graphene to obtain the improvement in K_{Ic} or G_{Ic} achieved in this study.[6,13] **Figure 12** clearly shows that compared to carbon nanotubes and nanoclays, graphene materials exhibit better performance in toughening epoxy, and with optimized surface functionalization and processing as shown in this study, the toughening effect of graphene materials can be further improved.

2.5. Toughening Mechanism at Small Graphene Loadings

The failure of polymers is a very complicated process and involves the loss of structural integrity at microscopic and macroscopic levels under deformation. Istrate et al. reported the toughening of semicrystalline PET by 0.07 wt% of graphene, which was attributed to the reinforcement of the stress-induced crystallites by graphene.[9] However, in highly crosslinked, brittle epoxies, the influence of graphene on the fracture process may be different from the case of semicrystalline polymers. The intrinsic brittleness of neat epoxy polymers results in catastrophic fracture because of the lack of energy-absorbing events during the crack propagation. Inclusion of a secondary rubbery phase in the crosslinked structure has shown great effectiveness, because the yielding of the rubbery phase during debonding with the matrix can dissipate a significant amount of energy leading to an increase in the toughness.[1,23] However, for epoxies filled with inorganic particles, due to the high rigidity of the filler particles, the toughening mechanism involves the plastic yielding of the matrix around particles and subsequent void formation, as well as the interference of rigid particles during crack propagation, such as crack deflection and crack pinning (schematic illustrations in Figure S4 and proposed fracture toughening mechanisms in Table S3 in Supporting Information).[4,10] When the crack front encounters a rigid particle, the crack plane can be deflected by tilting or twisting, and thus a larger crack area results compared to undeflected propagation. The crack tip can also be pinned by the particulate obstacles, and thus the crack length will be increased. Tails are usually formed behind the particles before the unification of the pinned crack into the primary crack plane, contributing to an increase in fracture line energy. Rigid fillers act as stress concentrators; the localized stress field surrounding a filler particle may form a microcrack zone and cause debonding between the particle and the matrix. Thus a microvoid forms around the particle in front of the crack tip opening, initiating the secondary crack propagation. Various studies have proposed that crack pinning and debonding effects are the two main mechanisms contributing to the overall toughening effect.[4,24]

Table 2. Graphene weight fraction, glass transition temperatures, T_g, from DSC analysis, *E″* peak and tan δ peak temperatures, and storage tensile moduli, *E′*, from DMA, of neat epoxy and epoxy/graphene nanocomposites.

Sample	Filler content [wt%]	DMA				DSC
		E′ at 30 °C [GPa]	*E′* at 100 °C [MPa]	T_g by max *E″* [°C]	T_g by max tan δ [°C]	T_g [°C]
E_Neat	0	2.47	15.8	73.8	83.1	75.1
E_GS2	0.08	2.53	16.2	74.6	84.2	76.8
	0.16	2.59	16.5	74.4	85.0	77.8
E_GO	0.08	2.42	15.8	76.1	84.2	81.2
	0.16	2.54	16.1	76.7	83.7	80.9
E_GA	0.08	2.57	16.2	72.6	83.2	76.0
	0.16	2.59	15.4	72.5	83.1	75.9

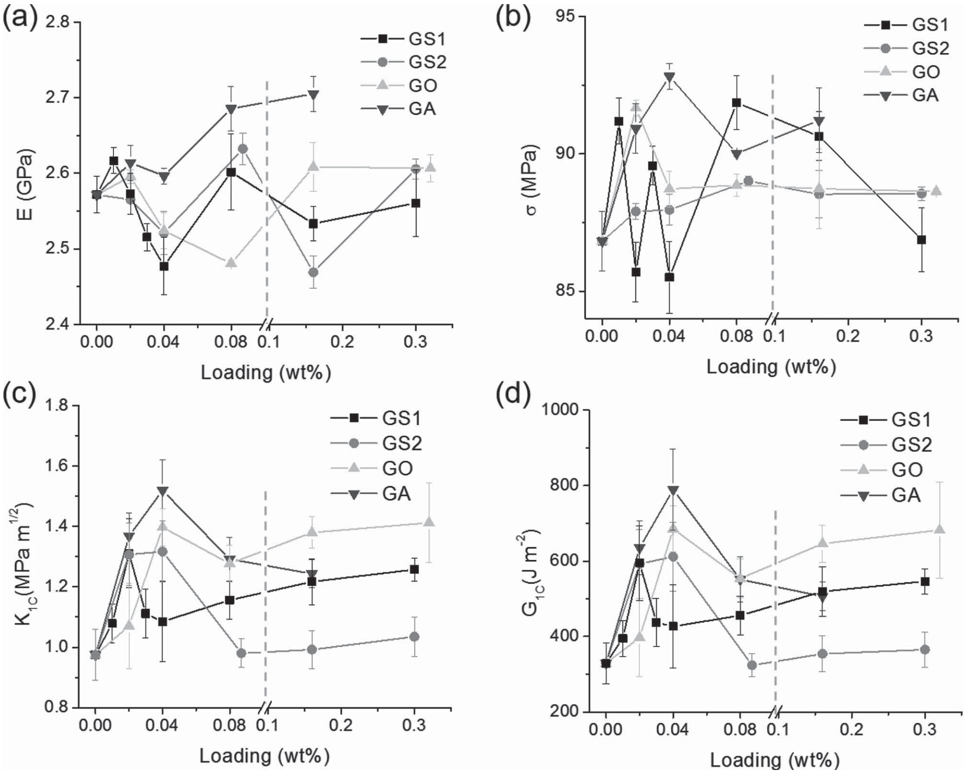

Figure 10. a) Flexural modulus, b) flexural strength, c) fracture toughness, and d) fracture energy plots of epoxy nanocomposites. Note the scale change in the *x*-axis as indicated by the dashed line.

SEM fractography was employed to investigate the fracture mechanism. The fractographs of neat epoxy and E_GS1 with different graphene loadings are shown in **Figure 13**. The neat epoxy displayed a very smooth fracture surface, and almost no events were observed during the crack propagation due to the brittleness of the matrix. After incorporation of GS1, some geometric markings were seen on the fracture surface. The "tail" morphology indicates that the marking was generated by crack pinning involving rigid GS1 particles. From the high magnification image in Figure 13e, microcracks were also observed around the particles, indicating the debonding between the graphene and the matrix. The amount of crack pinning and microcracks increased with higher GS1 loading (Figure 13c,d). At 0.16 wt% of GS1 loading, because of the short interparticle distances, the microcracks could be pinned again before they were unified into the primary crack. The crack deflection, pinning, and the coalescence of microcracks resulted in a very rough surface.

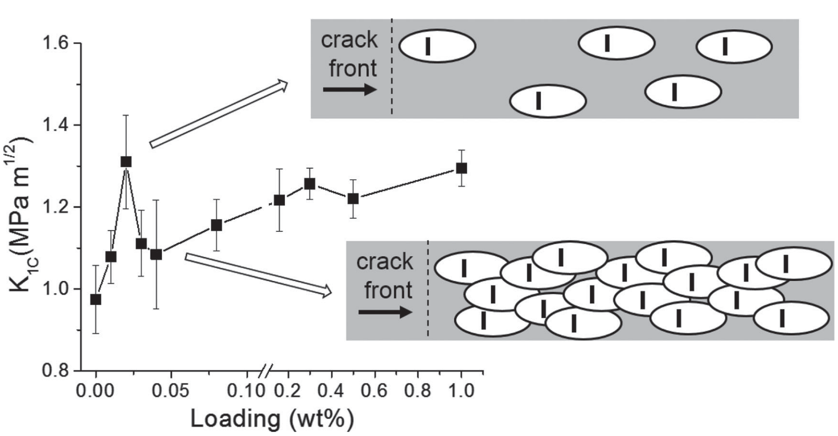

Figure 11. The correlation of the proposed microcrack mechanism to the K_{Ic} of E_GS1 at different graphene loadings. At 0.02 wt% loading, the microcracks can be independently distributed, whereas at loadings higher than 0.04 wt%, microcracks coalesce due to the short interparticle distance.

It is clear that at higher graphene loadings, crack deflection and crack pinning increase accordingly, which should result in an increase in fracture toughness. In our study, however, a peak in K_{Ic} at a small graphene loading was observed, followed by a decrease and then a slow increase of K_{Ic}. In a previous study, it was suggested that crack deflection was the main mechanism for the peak of K_{Ic} at small graphene loadings, and the subsequent decrease of K_{Ic} was attributed to the aggregation of graphene.[12] However, more crack deflections occurred in the composites with higher graphene loadings, and no significant aggregation of GS1 was observed in the composite with a higher loading (Figure S5,S9 in Supporting Information). In fact, preformed microvoids in epoxy with rigid plastic particles were reported to show toughening effects similar

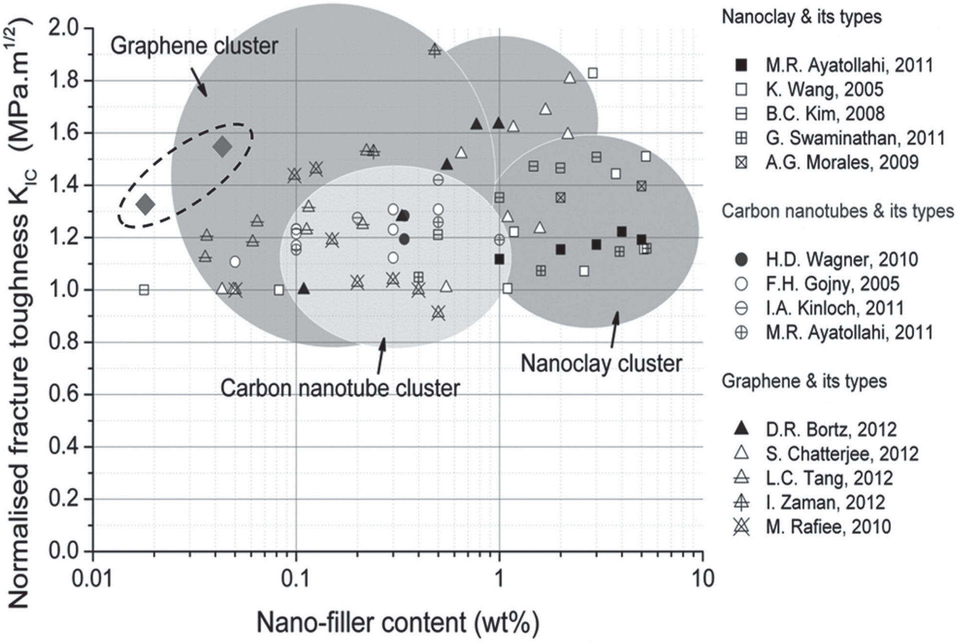

Figure 12. Normalized fracture toughness as a function of filler content for different nano-filler reinforced epoxies. Our results are shown as diamonds (♦) within the dashed circle. The other indicated references are provided in a previous study. Adapted with permission.[10] Copyright 2014, Elsevier.

to rubber tougheners.[25] On the other hand, if the microcrack zones are close to each other, the coalescence of microcracks may facilitate a major crack propagation. Therefore, we propose that microcrack formation contributes most to the maximum toughening at small graphene loadings, as shown in Figure 11. As the graphene loading increases, crack pinning and crack deflection become more important in the epoxy toughening. In this case, the trend for the increase in K_{Ic} on the graphene loading is less steep because the coalescing of microcracks may facilitate the propagation of the primary crack.

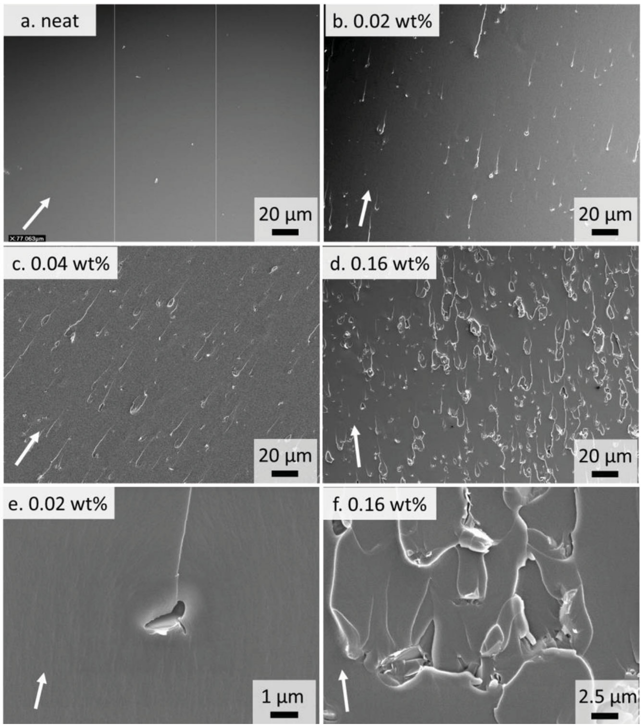

Figure 13. SEM fractographs of a) neat epoxy and E_GS1 composites at graphene loadings of b) 0.02 wt%, c) 0.04 wt%, d) 0.16 wt%. The images in (e,f) are higher magnification images for 0.02 wt% and 0.16 wt% loadings, respectively. White arrows indicate the crack propagation direction.

GS2 nanosheets are similar to GS1 in structure but much thinner. From **Figure 14**a we can see that the tails around the particles in E_GS2 are much shorter than those in E_GS1, possibly because thin GS2 sheets can be easily broken, and thus are not able to induce as effective microcrack formation and crack pinning as GS1. However, the number of GS2 particles is much greater than that of GS1 in the composite with the same graphene loading (Figure S10 in Supporting Information), so E_GS2 still exhibits significant toughening at graphene contents of 0.02 and 0.04 wt%. The coalescence of secondary microcracks in E_GS2 should follow a similar manner to that in E_GS1, causing the decrease of K_{Ic} after 0.04 wt%. With 0.16 wt% graphene, the surface roughness of E_GS2 is much less than that of E_GS1, indicating a lower K_{Ic} (Figure 10c).

According to the proposed microcrack mechanism for the epoxy toughening at small graphene loadings, if the energy consumption for the microcrack formation is higher, then higher fracture toughness should be observed. For E_GO and E_GA, the functional groups on GO and GA can induce a reaction between epoxy and graphene fillers during the curing process. The interfacial covalent bonding increases the energy dissipation to form microcracks, and therefore the corresponding composites exhibit higher fracture toughness than composites with pristine graphene. For E_GA, because the grafted rubber chain can further store elastic energy, the highest fracture toughness is observed. From the SEM images, deeper voids

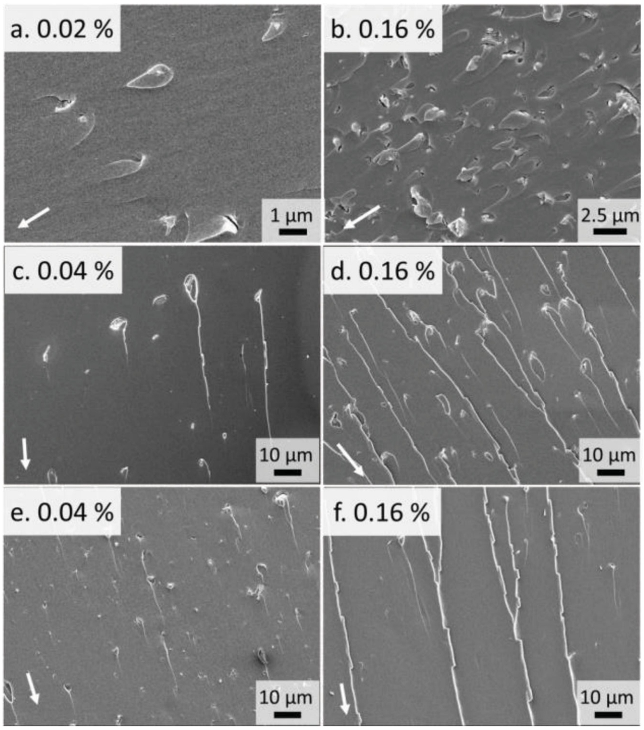

Figure 14. SEM fractographs of a,b) E_GS2, c,d) E_GO, and e,f) E_GA. Graphene loadings shown are weight%. White arrows indicate the crack propagation direction.

visible in the fracture surface morphology of E_GA compared to E_GS or E_GO indicated strong interfacial interactions in E_GA (see detailed images in Figure S11 in Supporting Information). The interfacial bonding also affected the morphology at higher graphene loadings. In Figure 14d,e, E_GO and E_GA displayed a pattern with stretched lines throughout the fracture surface, rather than a random coalescence of microcracks observed in the composites with pristine graphenes. Due to the covalent tethering to the filler particle, the epoxy matrix may undergo plastic yielding around GO or GA. During crack propagation, the matrix surrounding the graphene is pulled out to form the stretched lines in the same direction of crack propagation. The higher K_{Ic} values of E_GO compared to E_GS1 may be ascribed to the absence of significant coalescence of microcracks and the increase of the fracture line energy.

3. Conclusion

In this study, four types of graphene nanosheets were incorporated into an epoxy matrix via a facile, solvent-free route. GO was modified with ATBN molecules to improve the dispersion in epoxy and increase the interfacial strength. Good dispersions of graphene in the nanocomposites were demonstrated by TEM, except that some stacking of GO nanosheets was observed in the nanocomposites. An impressive toughening effect was observed for nanocomposites with less than 0.1 wt% of graphene, and epoxy composites with GA showed a 1.5-fold improvement in K_{Ic} and a corresponding 2.4-fold improvement in G_{Ic} at 0.04 wt% of graphene loading. No other study in the literature has achieved such high toughness at this low loading. Interestingly, all the composite systems showed a toughness peak at loadings as small as 0.02 or 0.04 wt%. From SEM fractography observations a microcrack-crazing mechanism was proposed to explain the fracture results. Due to the significant improvement in toughness at such small loading levels, this functionalized graphene approach is economically attractive.

4. Experimental Section

Materials: The following materials were used as received: Epon 828 epoxy resin (MW ~377 g mol^{-1}, Momentive), Jeffamine D230 curing agent (MW = 250 g mol^{-1}, Huntsman), 4,4′-methylene diphenyl diisocyanate (98%, Sigma-Aldrich), $NaNO_3$ and $KMnO_4$ (Fisher Scientific), concentrated H_2SO_4 and HCl (VWR International), H_2O_2 (30%, Macron Fine Chemicals). Two grades of pristine graphene nanosheets (Angstron Materials, see Table 1) were dried under vacuum at 70 °C overnight before use. Natural graphite flakes (SP-1, 45 µm, Bay Carbon) were used to prepare graphene oxide. Hycar 1300 × 42 primary amine-terminated poly(butadiene-acrylonitrile) (Emerald Performance Materials, MW = 3800 g mol^{-1} as specified on the technical data sheet) was also dried under vacuum before functionalization of graphene oxide. Dimethylformamide and dichloromethane were dried with molecular sieves before use.

Preparation of Graphene Oxide: GO was synthesized from natural graphite according to the Hummers method as reported elsewhere.[26] After the oxidation, excess oxidant was removed by washing with H_2O_2 solution (30 wt%), and the resulting slurry was centrifuged and washed with 2 M HCl until it was SO_4^{2-} free as tested by 0.1 M $BaCl_2$ solution. Then the brown dispersion was dialyzed several times in deionized water until the pH reached a value of ~3 and remained unchanged. The pH of the GO dispersion was adjusted to around 6 with NaOH solution, and then bath sonication was used to aid the exfoliation of GO. GO was obtained as a powder by freeze-drying the dialyzed solution and further drying in a vacuum oven at 60 °C overnight.

Preparation of ATBN-modified GO: ATBN chains were grafted onto GO by using MDI as the coupling agent, as illustrated in Figure 1. GO (200 mg) was dispersed in DMF (50 mL) by bath sonication. The dispersion was purged with nitrogen for 30 min, followed by addition of MDI (4 g). The reaction was carried out in an oil bath at 60 °C for 24 h, and then the mixture was flocculated by adding dichloromethane. The solid product was washed with dichloromethane at least five times to remove any excess MDI. The centrifuge tubes were sealed with parafilm to minimize exposure to moisture from the air. GO-NCO was dispersed in DMF (100 mL) without drying. After bath sonication, a solution of 10 wt% ATBN in DMF (20 g) was added while stirring. The reaction was carried out at 60 °C with nitrogen purging for two days. Acetone was used to flocculate the mixture, and the solid product was collected by centrifugation. After washing with acetone at least five times, GA was redispersed in *tert*-butanol, which was then freeze-dried. GA was obtained as a powder after freeze-drying further drying in a vacuum over at 60 °C for 6 h.

Synthesis of Epoxy/Graphene Nanocomposites: The desired amount of graphene nanofillers was first weighed and dispersed in Jeffamine D230 using an ultrasonic probe sonicator (Misonix S4000 with 0.25” microtip) for 3 h (90 °C for GS1 and GS2, 70 °C for GO and GA). After the D230-graphene dispersion had cooled down to room temperature, it was added to Epon 828 epoxy resin, which has been commonly used in previous nanocomposites studies,[6,27] and the mixture was mechanically stirred with a Cowles blade at 700 rpm for 2 min and then 300 rpm for 15 min. The amounts of epoxy resin and amine curing agent were 100 and 35 parts by weight, respectively. Next, the mixture was degassed for 15 min in a vacuum oven, followed by pouring into glass molds. The nanocomposites were obtained after curing at 60 °C for 2 h and 120 °C for another 12 h.

Characterization: Fourier transform-infrared spectroscopy was carried out using a Nicolet Magna-IR 760 spectrometer. X-ray diffraction patterns were acquired using a PANalytical X-Pert Pro MPD X-ray diffractometer equipped with a Co source (45 kV, 40 mA, $\lambda = 0.179$ nm) and an X-Celerator detector. Transmission electron microscopy images were obtained on a FEI Tecnai T12 microscope using an accelerating voltage of 100 kV. Graphene samples were picked up on carbon-coated Cu grids from dispersions. Polymer samples were first microtomed (Leica Ultracut) at room temperature into 70 nm thick sections before being picked up on Cu grids. Thermogravimetric analyses were carried out with a Netzsch STA 409 PC instrument in flowing nitrogen using a ramping rate of 10 °C mim^{-1}. Scanning electron microscopy images were taken using a JEOL 6500 FEG-SEM with an accelerating voltage of 5 kV. Samples were mounted on Al stubs, and a 5 nm Pt coating was applied on insulating samples. Rheological characteristics of the curing agent/graphene blends were measured using a AR-G2 (TA Instruments) rotational rheometer with a 40 mm cone plate at room temperature. Viscosity profiles were obtained under steady state flow as the shear rate was increased in logarithmic increments from 0.1 to 1000 s^{-1}. Thermo-mechanical properties of E_graphene composites were studied with a dynamic temperature ramp from 25 to 150 °C (ramping rate = 5 °C min^{-1}) using a RSA-G2 solids analyzer (TA Instruments). 3 mm wide and 4 cm long rectangular strips cut from the cured plates were dried in vacuum at room temperature and mounted between tensile fixtures. Dynamic tensile storage and loss moduli were measured at 1 rad s^{-1}. During each test, static pretension on the specimens was maintained at a frequency of 1 Hz under a dynamic strain of 0.004% with a pretension of 50 g force. DSC measurements were carried out with a TA Instruments DSC Q1000. A sample mass of 5 mg was loaded into an aluminum pan and scanning was performed from –10 °C to 200 °C at a rate of 10 °C min^{-1} after removing the thermal history with 5 min heating at 200 °C. The T_g determination was based on the inflection point method using TA Universal Analysis software. For mechanical testing, samples were cut into specimens with specific geometries as shown in Figure S12 (Supporting Information). Flexural modulus and strength were measured using an RSA-G2 solids analyzer (TA Instruments) according to ASTM D790–10 at a span-to-thickness ratio of 16 and a crosshead rate of 0.25 mm min^{-1} (0.01 min^{-1} strain rate). Fracture behavior was measured with crack-opening tests on compact tension specimens according to ASTM D5045–99. A precrack with an average length of 2 ± 0.6 mm was initiated by tapping a fresh liquid-N_2-chilled razor blade into the notch. Specimens were loaded to failure at 10 mm min^{-1} using an Instron 3344 single column testing system equipped with a 5 kN load cell. At each weight fraction of graphene additives, we tested 15 different samples to check for reproducibility of the results, and then the mode-I critical-stress-intensity factor (K_{Ic}) and critical strain energy release rate (G_{Ic}) were calculated based on Equation 1 and 3, respectively. The mode-I critical-stress-intensity factor is defined as

$$K_{\text{Ic}} = \frac{P_{\text{Q}}}{B\sqrt{W}} f(x) \tag{1}$$

where P_{Q} is the maximum loading force in the compact-tension test, B and W are sample thickness and characteristic length of the specimen, respectively, as defined in Figure S12. $f(x)$ is the geometric factor, defined as

$$f(x) = \frac{(2+x)\left(0.886 + 4.64x - 13.22x^2 + 14.72x^3 - 5.6x^4\right)}{(1-x)^{3/2}} \tag{2}$$

where $x = a/W$ and a is the initial notch length including the precrack. The mode-I critical strain energy release rate is defined as

$$G_{\text{Ic}} = \frac{\left(1-\nu^2\right)K_{\text{Ic}}^2}{E} \tag{3}$$

where E is the elastic modulus and ν is the Poisson ratio of the epoxy, which is taken to be 0.34.[28]

Supporting Information

Supporting Information is available from the Wiley Online Library or from the author.

Acknowledgements

Y.T.P. and Y.Q. contributed equally to this work. The authors thank Adama Materials Inc. for providing financial support and Dr. Frank Thibodeau and Mr. Steven Speak for valuable discussions. Parts of this work were carried out at the University of Minnesota Characterization Facility, which receives partial support from the NSF through the NNIN program, and at the College of Science and Engineering Polymer Characterization Facility, University of Minnesota, which has received capital equipment funding from the NSF through the MRSEC program, Award DMR-0819885.

Received: July 29, 2014
Revised: October 29, 2014
Published online: December 6, 2014

---

[1] S. C. Kunz, J. A. Sayre, R. A. Assink, *Polymer* **1982**, *23*, 1897.

[2] a) A. F. Yee, R. A. Pearson, *J. Mater. Sci.* **1986**, *21*, 2462; b) J. Ma, M.-S. Mo, X.-S. Du, S.-R. Dai, I. Luck, *J. Appl. Polym. Sci.* **2008**, *110*, 304.

[3] a) A. J. Kinloch, M. L. Yuen, S. D. Jenkins, *J. Mater. Sci.* **1994**, *29*, 3781; b) J. Dean, P. Lipic, R. Grubbs, R. Cook, F. Bates, *J. Polym. Sci., Part B: Polym. Phys.* **2001**, *39*, 2996; c) Z. J. Thompson, M. A. Hillmyer, J. Liu, H. J. Sue, M. Dettloff, F. S. Bates, *Macromolecules* **2009**, *42*, 2333.

[4] a) B. Wetzel, P. Rosso, F. Haupert, K. Friedrich, *Eng. Fract. Mech.* **2006**, *73*, 2375; b) B. B. Johnsen, A. J. Kinloch, R. D. Mohammed, A. C. Taylor, S. Sprenger, *Polymer* **2007**, *48*, 530; c) P. Dittanet, R. A. Pearson, *Polymer* **2013**, *54*, 1832.

[5] a) K. Wang, L. Chen, J. Wu, M. L. Toh, C. He, A. F. Yee, *Macromolecules* **2005**, *38*, 788; b) B. C. Kim, S. W. Park, D. G. Lee, *Compos. Struct.* **2008**, *86*, 69; c) F. Gojny, M. Wichmann, U. Köpke, B. Fiedler, K. Schulte, *Compos. Sci. Technol.* **2004**, *64*, 2363; d) N. Lachman, H. Daniel Wagner, *Compos. Part A* **2010**, *41*, 1093; e) T. H. Hsieh, A. J. Kinloch, A. C. Taylor, I. A. Kinloch, *J. Mater. Sci.* **2011**, *46*, 7525.

[6] I. Zaman, T. T. Phan, H. C. Kuan, Q. S. Meng, L. T. B. La, L. Luong, O. Youssf, J. Ma, *Polymer* **2011**, *52*, 1603.

[7] a) S. Stankovich, D. A. Dikin, G. H. B. Dommett, K. M. Kohlhaas, E. J. Zimney, E. A. Stach, R. D. Piner, S. T. Nguyen, R. S. Ruoff, *Nature* **2006**, *442*, 282; b) K. H. Liao, Y. Q. Qian, C. W. Macosko, *Polymer* **2012**, *53*, 3756; c) K.-H. Liao, Y. T. Park, A. Abdala, C. Macosko, *Polymer* **2013**, *54*, 4555.

[8] a) A. K. Geim, *Science* **2009**, *324*, 1530; b) Y. Qian, A. Vu, W. Smyrl, A. Stein, *J. Electrochem. Soc.* **2012**, *159*, A1135; c) H. Kim, A. A. Abdala, C. W. Macosko, *Macromolecules* **2010**, *43*, 6515; d) A. Zandiatashbar, G.-H. Lee, S. J. An, S. Lee, N. Mathew, M. Terrones, T. Hayashi, C. R. Picu, J. Hone, N. Koratkar, *Nat. Commun.* **2014**, *5*, 3186.

[9] a) K. P. Pramoda, H. Hussain, H. M. Koh, H. R. Tan, C. B. He, *J. Polym. Sci., Part B: Polym. Phys.* **2010**, *48*, 4262; b) O. M. Istrate, K. R. Paton, U. Khan, A. O'Neill, A. P. Bell, J. N. Coleman, *Carbon* **2014**, *78*, 243.

[10] S. Chandrasekaran, N. Sato, F. Tölle, R. Mülhaupt, B. Fiedler, K. Schulte, *Compos. Sci. Technol.* **2014**, *97*, 90.

[11] M. A. Rafiee, J. Rafiee, Z. Wang, H. H. Song, Z. Z. Yu, N. Koratkar, *ACS Nano* **2009**, *3*, 3884.

[12] M. A. Rafiee, J. Rafiee, I. Srivastava, Z. Wang, H. H. Song, Z. Z. Yu, N. Koratkar, *Small* **2010**, *6*, 179.

[13] a) J. Ma, Q. S. Meng, A. Michelmore, N. Kawashima, Z. Izzuddin, C. Bengtsson, H. C. Kuan, *J. Mater. Chem. A* **2013**, *1*, 4255; b) D. R. Bortz, E. G. Heras, I. Martin-Gullon, *Macromolecules* **2012**, *45*, 238.

[14] R. Russ, M. Ghasemi-Nejhad, A. Tiwari, A. Chaturvedi, D. A. Hummer, V. Gudapati, *WO 2011120008 A1*, **2011**.

[15] D. R. Dreyer, S. Park, C. W. Bielawski, R. S. Ruoff, *Chem. Soc. Rev.* **2010**, *39*, 228.

[16] K.-H. Liao, A. Mittal, S. Bose, C. Leighton, K. A. Mkhoyan, C. W. Macosko, *ACS Nano* **2011**, *5*, 1253.

[17] W. J. Li, X. Z. Tang, H. B. Zhang, Z. G. Jiang, Z. Z. Yu, X. S. Du, Y. W. Mai, *Carbon* **2011**, *49*, 4724.

[18] a) S. Stankovich, R. D. Piner, S. T. Nguyen, R. S. Ruoff, *Carbon* **2006**, *44*, 3342; b) C. Xu, X. Wu, J. Zhu, X. Wang, *Carbon* **2008**, *46*, 386.

[19] D. A. Dikin, S. Stankovich, E. J. Zimney, R. D. Piner, G. H. Dommett, G. Evmenenko, S. T. Nguyen, R. S. Ruoff, *Nature* **2007**, *448*, 457.

[20] W. Abdelwahed, G. Degobert, S. Stainmesse, H. Fessi, *Adv. Drug Delivery Rev.* **2006**, *58*, 1688.

[21] a) Y. Qian, W. Liu, Y. T. Park, C. I. Lindsay, R. Camargo, C. W. Macosko, A. Stein, *Polymer* **2012**, *53*, 5060; b) Y. Qian, C. I. Lindsay, C. Macosko, A. Stein, *ACS Appl. Mater. Interfaces* **2011**, *3*, 3709; c) Y. T. Park, Y. Qian, C. I. Lindsay, C. Nijs, R. E. Camargo, A. Stein, C. W. Macosko, *ACS Appl. Mat. Interfaces* **2013**, *5*, 3054.

[22] a) T. Mori, K. Tanaka, *Acta Metall.* **1973**, *21*, 571; b) G. P. Tandon, G. J. Weng, *Polym. Compos.* **1984**, *5*, 327.

[23] a) R. Bagheri, B. Marouf, R. Pearson, *J. Macromol. Sci., Part C: Polym. Rev.* **2009**, *49*, 201; b) C. Declet-Perez, E. M. Redline, L. F. Francis, F. S. Bates, *ACS Macro Lett.* **2012**, *1*, 338.

[24] J. Ma, M.-S. Mo, X.-S. Du, P. Rosso, K. Friedrich, H.-C. Kuan, *Polymer* **2008**, *49*, 3510.

[25] R. Bagheri, R. A. Pearson, *Polymer* **1995**, *36*, 4883.

[26] a) W. S. Hummers, R. E. Offeman, *J. Am. Chem. Soc.* **1958**, *80*, 1339; b) Y. Qian, I. M. Ismail, A. Stein, *Carbon* **2014**, *68*, 221.

[27] Q.-H. Le, H.-C. Kuan, J.-B. Dai, I. Zaman, L. Luong, J. Ma, *Polymer* **2010**, *51*, 4867.

[28] A. Netravali, R. Henstenburg, S. Phoenix, P. Schwartz, *Polym. Compos.* **1989**, *10*, 226.